Research Article Vol. 11, No. 11 / November 2024 / Optica 1567

Single-mode chirped high-contrast metastructure VCSEL for 106 Gbps PAM4 transmission

Yao Cui,[1,2] Huawen Hu,[2] Yipeng Ji,[2] Jonas Kapraun,[2] Jiaxing Wang,[2] Xuanlun Huang,[2,3] and Connie J. Chang-Hasnain[1,2,3,*]

[1]Tsinghua-Berkeley Shenzhen Institute, Tsinghua University, Shenzhen 518055, China
[2]Berxel Photonics Co. Ltd., Shenzhen 518055, China
[3]School of Information Science and Technology, Fudan University, Shanghai 200433, China
*connie.chang@berxel.com

Received 14 August 2024; revised 14 October 2024; accepted 15 October 2024; published 13 November 2024

Short-reach optical interconnects, employing an 850 nm wavelength multimode vertical cavity surface emitting laser (VCSEL) and multimode fiber (MMF), are confronted with transmission distance limitation as the transmission speed increases. Achieving higher speeds over the same transmission distance necessitates a significant enhancement in the fiber's effective bandwidth, resulting in substantial costs. Employing single-mode VCSEL with single-mode fiber transmission presents as a more economically viable solution. Here we report, to our knowledge, the first demonstration of an 850 nm single-mode VCSEL using a chirped high-contrast metastructure (HCM) as the top mirror with spatially graded reflectivity to suppress higher-order modes. The chirped HCM top reflector is designed to favor lasing of the fundamental mode. We show stable single-mode lasing with a >40 dB side mode suppression ratio (SMSR) up to 15 times threshold current and an open eye through a short single-mode fiber SM800 transmission at 106 Gbps PAM4 modulation. This study highlights the potential for scalable single-mode VCSEL in advanced optical interconnects, providing a cost-effective pathway for high-speed applications.

https://doi.org/10.1364/OPTICA.539252

1. INTRODUCTION

A multimode vertical cavity surface emitting laser (VCSEL) and multimode fiber (MMF) links operating at an 850 nm wavelength window are attractive for short-reach optical interconnects used in data centers and super computers due to their low power consumption and cost effectiveness [1]. Recently, the exponential growth of data center traffic has created increasing demands for higher data rates and the move to 100 Gbps per channel to support growing applications such as multimedia-rich networks, cloud computing, and hyper-scale metadata analytics. The transmission distance in multimode fibers is limited, particularly at high data rates of 100 Gbps PAM4 and beyond. This limitation stems from the fiber's effective bandwidth being constrained by the chromatic dispersion experienced by signals from multimode VCSEL and modal dispersion of the multimode fiber [2]. The requirements and costs associated with multimode fiber technology are high, especially for achieving 100 Gbps; and OM4 or OM5 fibers are necessary [3,4]. Alternatively, employing single-mode VCSEL with single-mode fiber transmission could be a more cost-effective solution [5–7].

There have been various approaches reported to achieve single-mode 850 nm VCSEL. The most direct method involves reducing the aperture size to 3–4 μm in order to maintain single-mode operation [8–10]. Other strategies involve enhancing the disparity in modal gain between the fundamental mode and higher-order modes through techniques such as employing tunnel junctions [11,12], implementing hybrid radial confinements of an optical field and current spreading [13,14], and utilizing disordered quantum-well structures [15] or coupled cavity designs [16–18]. Alternatively, other approaches aim to augment the discrepancy in modal losses between the fundamental mode and higher-order modes by leveraging mirror loss [19–24], absorption loss [25,26], diffraction loss [27–29], and scattering loss [30,31].

All these approaches suffer from certain drawbacks. The small aperture devices suffer from drawbacks such as low electro-static discharge (ESD) voltage, reduced reliability, high ohmic resistance, and limited optical output power [32,33]. The larger aperture ones involve complex structures and require multiple process steps or growth interruption and regrowth steps, which hinder low-cost and high-yield manufacturing processes. Finally, for real world applications, single-mode operation with a high side mode suppression ratio (SMSR) must be maintained over a wide range of bias current, from threshold to typically 8 mA, and over a wide temperature range, from 5°C to 75°C substrate temperature. In addition, the VCSEL must be able to have an ESD limit greater than 100 V (Telcordia Standards).

High-index-contrast near wavelength dielectric structure, also known as high-contrast metastructure (HCM), is a type of metastructure that surrounds the high-index medium with low-index

materials [34]. In recent years, HCMs have garnered significant attention due to their ultrathin structure, low absorption loss, and exceptional light manipulation capabilities. These novel designs utilizing HCMs have found applications in various photonic devices such as holograms, spatial light modulators, waveguides, couplers, reconfigurable optics, ultrabroadband high-reflectivity mirrors, and high-quality-factor resonators [35,36]. HCMs are particularly suitable for serving as top mirrors in VCSEL to replace conventional distributed Bragg reflectors (DBRs) and create structurally sampled configurations [37,38]. Furthermore, the modal losses can be controlled by designing different reflectivity across the aperture to achieve single-mode output. The proposed approach, which solely modifies the topmost structure instead of making modifications inside the VCSEL like many other methods aiming for single-mode operation, exhibits enhanced simplicity and improved reliability. Despite its ease of implementation for practical applications in obtaining single-mode VCSEL, using HCM remains an unexplored area in current literature.

Here we present, for the first time, to our knowledge, an 850 nm single-mode VCSEL using HCM working as the top mirror to achieve a gradient in reflectivity. By precisely adjusting the dimensions of the HCM, the reflectivity can be spatially tailored to the intensity profile of the fundamental mode in transverse direction. An HCM top mirror designed in such way effectively supports the fundamental mode while suppressing higher-order modes. Leveraging state of the art III-V fabrication techniques, the 850 nm VCSEL reported here achieves single-mode emission with a side mode suppression ratio (SMSR) of >40 dB over a large current and temperature range with a 6 μm aperture. The device has an ESD limit of larger than 125 V. These devices are capable of 100 Gbps PAM4 modulation and signal transmission through a single-mode fiber SM800. Therefore, the integration of these single-mode VCSELs with a single-mode fiber technique holds significant potential for future data centers, offering enhanced speed and cost effectiveness.

2. STRUCTURE AND DESIGN

The operational principle of our single-mode VCSEL with chirped HCM is based on the adjustment of modal loss for different modes. When a wave is incident upon chirped HCM, the reflectivity varies along the x and y axes due to the chirp in the HCM dimensions. By appropriately designing the reflectivity distribution along the x/y axis, it is possible to achieve a gradual drop in the reflectivity of the top mirror that matches the intensity profile of the fundamental mode from the center of the aperture to the edge (in transverse direction), thereby effectively supporting the fundamental mode, while suppressing the higher-order transverse modes. The subsequent paragraphs provide further elaboration on the simulation and design of chirped HCM.

The schematic of our GaAs-based chirped HCM VCSEL is presented in Fig. 1, which has a structure similar to that reported previously and is fabricated using selective oxidation [39]. The spacer between the HCM and the rest of the structure comprises AlGaAs with a sufficiently high Al content, facilitating oxidation to generate the low-index Al_2O_3 material beneath the HCM. This refractive-index contrast is sufficient to achieve a highly reflective mirror capable of supporting low-threshold lasing. The device comprises an active region sandwiched between a bottom mirror and a hybrid top mirror. The bottom mirror consists of 40 pairs of n-doped distributed Bragg reflectors (DBRs), while the hybrid top mirror is composed of a chirped HCM reflector and a few pairs of p-doped DBRs. The inclusion of the p-DBR facilitates current spreading and contributes to broader band top mirror reflectivity, enhancing robustness with respect to HCM dimensions. Notably, the chirped HCM is the primary determinant of the overall reflectivity of the top mirror. In particular, the HCM realizes the desired spatial reflectivity profile across the aperture to suppress higher-order modes. Electrical injection is achieved through a ring-shaped p-contact on the top side and a n-contact on the bottom side, utilizing an oxide aperture for both current and optical confinement within the VCSEL structure. Further details regarding the laser epitaxial structure and fabrication process can be found in Section 3.

In accordance with fundamental laser physics, a specific transverse LP_{ij} cavity mode is stimulated within a laser cavity when its modal gain G_{ij} reaches both its threshold value G_{ij}^{th} and matches the modal losses A_{ij}. For a given operating current J and each transverse mode LP_{ij}, the modal losses A_{ij} are defined as the average optical losses within the laser cavity weighted by the intensity distribution of the mode. Assuming cylindrical symmetry of the cavity, A_{ij} can be expressed as follows:

$$A_{ij} = \frac{\int_0^{2\pi} \mathrm{d}\varphi \int_0^L \mathrm{d}z \int_0^R I_{ij}(r, z, \varphi)\, \alpha(r, z, \varphi)\, r\,\mathrm{d}r}{\int_0^{2\pi} \mathrm{d}\varphi \int_0^L \mathrm{d}z \int_0^R I_{ij}(r, z, \varphi)\, r\,\mathrm{d}r}. \quad (1)$$

The radial, longitudinal, and azimuthal distributions of the LP_{ij} radiation mode intensity within a laser cavity are represented by $I_{ij}(r, z, \varphi)$, while the analogous distributions of optical losses are denoted as $\alpha(r, z, \varphi)$. Here, L represents the cavity length and R is the radius of the structure. The integral in the enumerator of Eq. (1) only has non-zero z values corresponding to different areas of radiation losses such as reflections from layer boundaries (including resonator mirrors), free carrier absorption, inter valence or band-to-band absorption beyond the active region, as well as scattering and diffraction losses. The focus of this paper specifically is on the mirror loss α_m governed by the chirped HCM, thereby enabling the optical losses α to be expressed as follows:

$$\alpha(r, z, \varphi) = \alpha_m(r, z_0, \varphi) = \frac{1}{2L} \ln \frac{1}{R(r, z_0, \varphi)}, \quad (2)$$

where z_0 represents the z-coordinate of chirped HCM, and $R(r, z_0, \varphi)$ denotes the radial and azimuthal distribution of power reflectivity induced by chirped HCM at z_0. Since different LP_{ij} modes exhibit varying intensities within the cavity, in accordance with Eqs. (1) and (2), to achieve single-mode output, it is crucial to minimize the loss A_{ij} experienced by the fundamental mode, while maximizing it for all higher-order modes. Therefore, minimizing reflectivity $R(r, z_0, \varphi)$ in locations where higher-order modes have a high intensity $I_{ij}(r, z, \varphi)$ is essential, whereas the opposite holds true for the fundamental mode. By implementing this strategy, higher-order modes are unable to reach their modal threshold gain G_{ij}^{th}, do not start to lase, and consequently enable the VCSEL to exclusively emit light from the fundamental mode.

The rigorous coupled-wave analysis (RCWA) method is employed to calculate the performance of the chirped HCM structure. The chirped HCM can be obtained from the 1D uniform HCM (also called high-contrast grating, HCG [36]) by adjusting the bar width and air gap within each period. In this study, our focus lies on the scenario where the period Λ remains constant while varying the duty cycle (DC), which is defined as

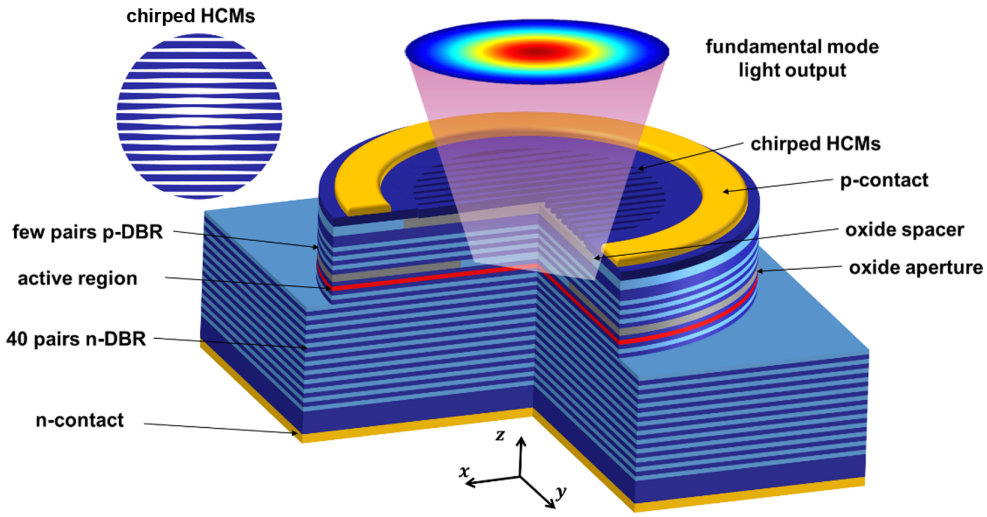

Fig. 1. Schematic of the proposed VCSEL featuring chirped HCM as the top reflector to facilitate fundamental mode lasing; the top-left inset shows a top view of the chirped HCM structure.

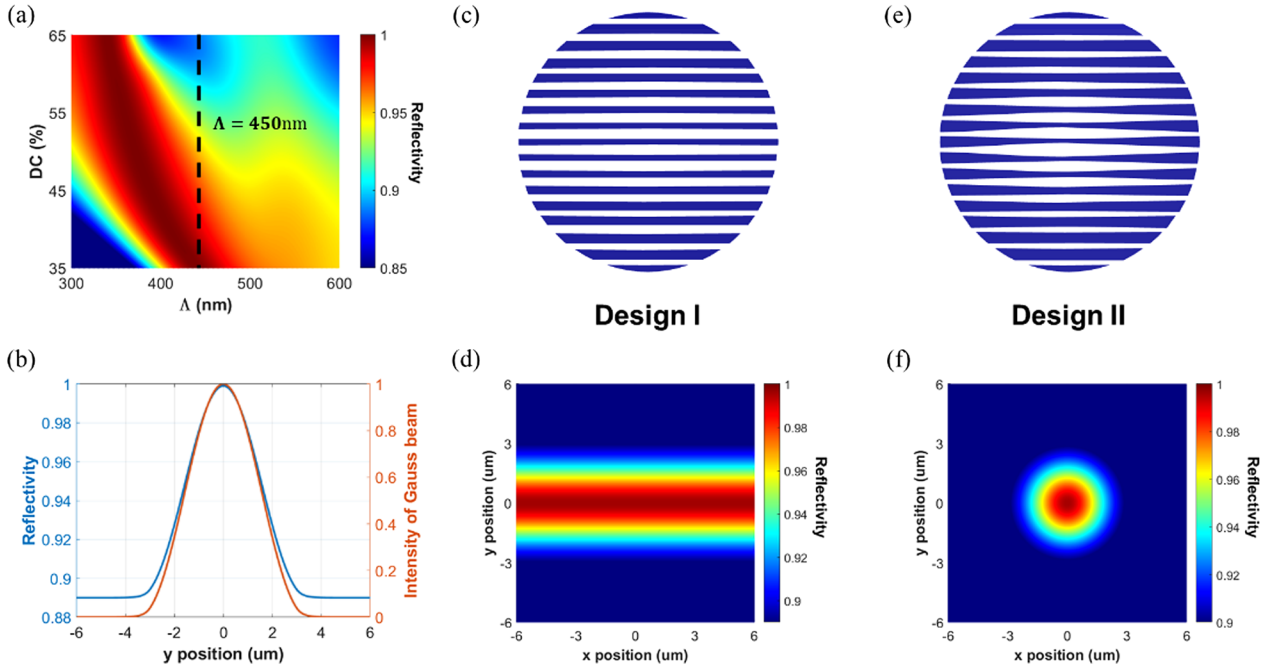

Fig. 2. (a) Reflectivity contours of the 1D uniform HCM as functions of period (Λ) and duty cycle (DC) for the TM incident case. (b) Reflectivity versus radial position at a fixed period of $\Lambda = 450$ nm, and intensity of Gaussian beam versus y position ($x = 0$). (c) Top view of design I: 1D chirped HCM structure and (e) design II: 2D chirped HCM structure. Reflectivity distribution in x/y positions is shown in (d) for design I and (f) for design II.

the ratio of bar width to period. Figure 2(a) shows the reflectivity contours of the 1D uniform HCM as functions of period (Λ) and duty cycle (DC) for the transverse magnetic (TM) incident case. It can be observed that the reflectivity varies continuously from 99.9% to 89% as the DC changes at a fixed period of $\Lambda = 450$ nm. Figure 2(b) presents the reflectivity and intensity of the fundamental mode (Gaussian beam) as a function of the y position (with $x = 0$), for an oxidized aperture (OA) size of 6 μm. The reflectivity profile follows a similar trend to the intensity of the fundamental mode, indicating effective support for the fundamental mode while suppressing higher-order modes. This is attributed to the lower optical losses of the fundamental mode compared to the higher-order modes. Figures 2(c) and 2(e) depict the top views of design I (1D chirped HCM structure) and design II (2D chirped HCM structure), respectively. Figures 2(d) and 2(f) show the reflectivity distribution in the x/y plane, with design I utilizing reflectivity to constrain modal loss in the one-dimensional direction and design II in the two-dimensional direction. For detailed chirped HCM dimensions designed to maximize the modal loss between the fundamental and higher-order modes, refer to Supplement 1, Part 1.

3. FABRICATION

The epitaxial structure is grown on a GaAs substrate of (100) lattice orientation using metal-organic chemical vapor deposition (MOCVD). The epitaxial growth comprises 40 pairs of

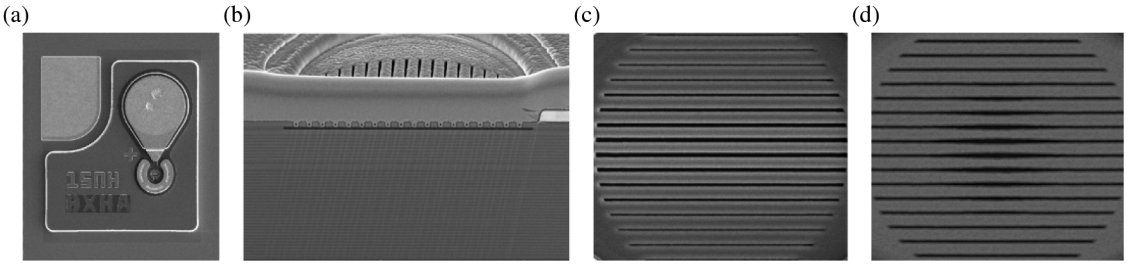

Fig. 3. (a) SEM (scanning electron microscopy) image of chirped HCM VCSEL chips at low magnification. (b) SEM cross-sectional image of a typical chirped HCM, showing a thick layer of Pt used as a protective layer during FIB (focused ion beam) processing. SEM top-view images of typical design I 1D (c) and design II 2D (d) chirped HCM, both protected by a 65 nm aluminum oxide coating applied through atomic layer deposition (ALD).

n-doped Si:AlGaAs DBRs, multiple InGaAs strained quantum wells employed as the active region, a single high-Al oxide layer with a purity of 98%, a few pairs of C:AlGaAs DBRs, a C:AlGaAs oxide spacer layer, and an HCM epitaxial layer on an n+ -GaAs substrate. The structure of the HCM layer follows our previous work [39].

The fabrication process comprises multiple steps, including HCM definition, oxide spacer formation, trench etching, oxide aperture formation, and metal contact depositions. Initially, the chirped HCMs are patterned on the top GaAs layer of the VCSEL epitaxial structure using electron-beam lithography (EBL) and chlorine-based inductively coupled plasma (ICP) etching down to the oxide spacer layer. Subsequently, a wet oxidation step is performed to selectively oxidize the aluminum-rich layer beneath the HCM and form a low-refractive-index oxide spacer. To prevent unintentional oxidation, a layer of Al_2O_3 is deposited atop the sample through atomic layer deposition (ALD).

The fabrication of oxide-aperture-confined VCSEL involves the utilization of standard VCSEL processing techniques. Trenches, with a depth of 2.5 μm, are defined through lithography and ICP etching to expose an additional aluminum-rich layer. This layer is then selectively oxidized via wet oxidation, the oxidation aperture is set to 6 μm and examined using an infrared camera system.

A passivation layer consisting of a deposition of aluminum oxide through ALD is applied; the ALD aluminum oxide layer is subsequently opened using buffered oxide etch, revealing a ring-shaped area that facilitates effective electrical access during contact formation. Finally, p-type contacts are patterned by depositing Ti/Au metals on both the top and bottom sides of the chip using electron-beam evaporation followed by a lift-off process.

Figure 3 presents various SEM (scanning electron microscopy) images of chirped HCM VCSEL chips. Figure 3(a) shows the chirped HCM VCSEL chips neatly arranged on a 6-inch wafer, illustrating the uniform arrangement and precision of the fabrication process. Figure 3(b) provides a cross-sectional view of a typical chirped HCM, where a thick platinum (Pt) layer is used as a protective layer above the chirped HCM VCSEL during FIB (focused ion beam) processing. Figures 3(c) and 3(d) display top-view SEM images of typical design I 1D and design II 2D chirped HCM, respectively, both protected by aluminum oxide coating applied through ALD. These images demonstrate the detailed structural features and protective measures implemented in the fabrication process.

4. EXPERIMENTAL RESULTS

Single-mode lasing from a chirped HCM VCSEL with graded top mirror reflectivity has been demonstrated for the first time, to the best of our knowledge. The L-I-V characteristics of these chirped HCM VCSELs were measured on a 6-inch quarter wafer using a probing system. Figure 4 compares the continuous wave (CW) performance of design I 1D and design II 2D chirped HCM VCSEL. The L-I-V curves at different temperatures (25°C, 50°C, 75°C; data for 5°C is missing as our L-I-V test stage lacks a refrigeration system) in Figs. 4(a) and 4(d) show that design I achieves an optical power output of 3.0 mW at 8 mA, while design II achieves 2.7 mW at 8 mA at 25°C. Both designs exhibit a Gaussian mode distribution in the far-field pattern at 8 mA, as shown in the bottom right corners. The threshold current (I_{th}) for design I is approximately 0.5 mA, while for design II it is slightly higher at around 0.7 mA.

The spectral characteristics of these chirped HCM VCSELs were analyzed under CW operation using a spectrometer with a high resolution of 0.02 nm. As shown in Figs. 4(b) and 4(e), the spectra of designs I and II at different currents at room temperature (25°C) demonstrate remarkable consistency in single-mode output. Design I achieves an SMSR of 37.5 dB at 8 mA, whereas design II achieves a higher SMSR of 43.2 dB at 8 mA. Figures 4(c) and 4(f) depict the spectra of designs I and II under different temperatures at a constant current of 8 mA. Notably, even at elevated temperatures, such as 75°C, both designs maintain excellent single-mode output consistency. Design I achieves an SMSR of 35.6 dB, while design II achieves an SMSR of 40.5 dB at this operating point.

The actual structure of the fabricated chirped HCM VCSEL may deviate from the designed values due to certain imperfections. These include dimensional shifts in the chirped HCM caused by ICP etching, lateral misalignment of the chirped HCM with the cavity's radial center due to EBL misalignment, and vertical misalignment resulting from less precise MOCVD growth. To address these dimensional shifts, we developed five different dimensions by varying the duty cycle of the chirped HCM, while keeping the HCM period (Λ) fixed for both design I and design II, with a 10 nm difference in each dimension. In each design, the reflectivity distribution across the oxide aperture (OA) follows the trend of the fundamental mode intensity, aimed at maximizing the modal loss difference between the higher-order modes and the fundamental mode. The results showed that most dimensions performed well, indicating good tolerance to these shifts. Detailed information can be found in Supplement 1, Part 2. Additionally, simulations were conducted to evaluate the impact of lateral and vertical misalignments, which showed limited influence. Further details are provided in Supplement 1, Part 3.

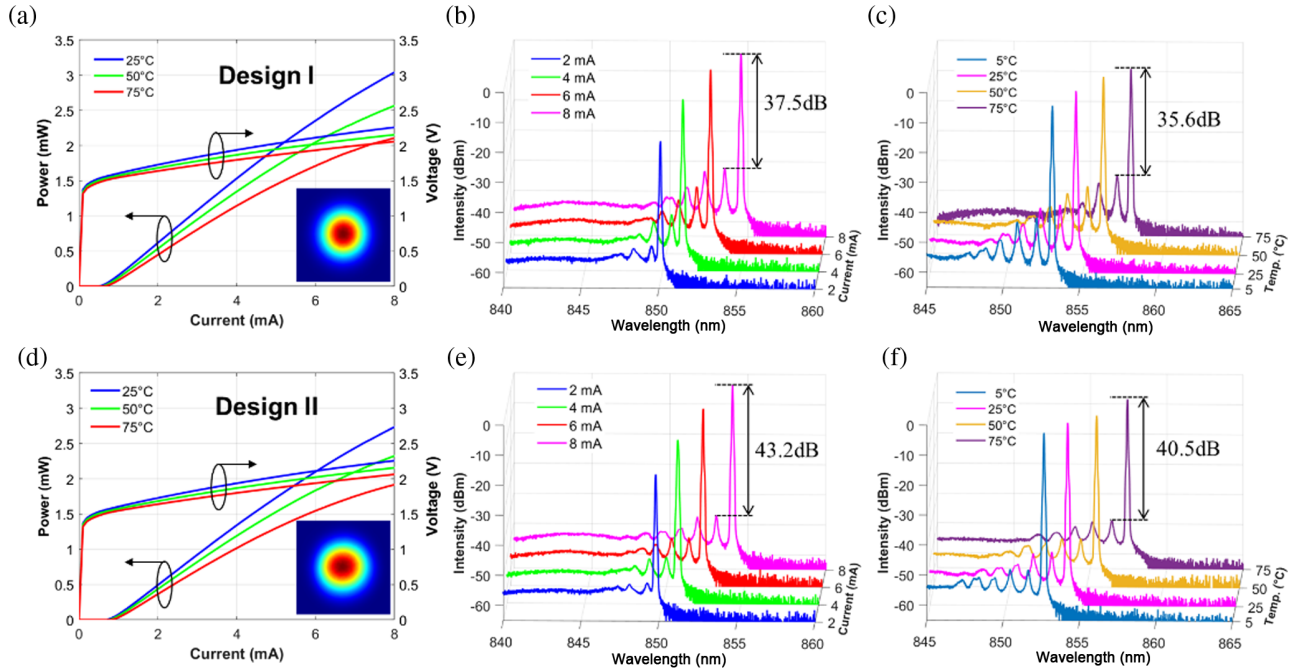

Fig. 4. Compares the L-I-V and spectrum performance of design I 1D and design II 2D chirped HCM VCSEL. (a), (d) L-I-V curves at different temperatures (25°C, 50°C, 75°C) show that design I achieves 3.0 mW at 8 mA, while design II achieves 2.7 mW at 8 mA at 25°C. Both designs exhibit a Gaussian mode distribution in the far-field pattern at 8 mA, as shown in the bottom right corners. (b), (e) Spectra at different currents at 25°C reveal that design I maintains an SMSR of 37.5 dB at 8 mA, whereas design II achieves a higher SMSR of 43.2 dB at 8 mA. (c), (f) Spectra at different temperatures at 8 mA show that design I reaches an SMSR of 35.6 dB at 75°C, while design II achieves 40.5 dB at 75°C. Overall, design I maintains a slightly higher power output, while design II exhibits better spectral purity with higher SMSR values.

Overall, design I maintains a slightly higher power output, while design II exhibits better spectral purity with higher SMSR values because design II matches the intensity profile of the fundamental mode from the center of the aperture to the edge in both x and y directions, while design I only matches the y direction (transverse direction).

The small-signal modulation response (S21) was measured using a 40 GHz photodetector and a 44 GHz vector network analyzer with the light from the chirped HCM VCSEL coupled to a short single-mode fiber SM800. The results are shown in Figs. 5(a) and 5(d). At room temperature and 8 mA current, both design I and design II chirped HCM VCSELs reach a 3 dB bandwidth of 23.4 GHz, and the modulation response is damped and relatively flat.

The relative intensity noise (RIN) is a critical parameter that characterizes the stability and performance of the device. Measurements were conducted to evaluate RIN at various operating currents, and the results are presented in Figs. 5(b) and 5(e). At a maximum current of 8 mA, design I reached an RIN of approximately −144 dB/Hz, while design II reached approximately −142 dB/Hz, indicating low levels of noise, which are desirable for applications requiring high signal-to-noise ratios.

The investigation of large signal modulation of the chirped HCM VCSEL single-mode devices is conducted using single-mode fiber SM800. The modulated optical signal is coupled into a lensed standard single-mode fiber SM800 and then connected to the oscilloscope for eye diagram measurement. Eye diagrams of different transmission data rates ranging from 53 Gbps to 106 Gbps in PAM4 format were examined. A DC bias current of 8 mA was utilized, with an extinction ratio (ER) set at approximately 3 dB. A nine-tap equalizer (EQ) was employed. Even at a data rate of 106 Gbps, open eyes could be observed for both design I and design II, as depicted in Figs. 5(c) and 5(f). Design I achieved a TDECQ of 4.08 dB, while design II achieved a TDECQ of 3.24 dB at 106 Gbps.

We also applied the three-pole transfer function [Eq. (S1) in Supplement 1] to fit the measured modulation response, extracting key parameters such as the resonant frequency f_r, damping factor γ, and parasitic pole frequency f_p. The fit revealed that f_p is slightly low, at 15.9 GHz, which limits further improvement of the S21 3 dB bandwidth and hinders additional reduction of TDECQ, though the current TDECQ already meets the standard IEEE Std 802.3db-2022 requirements. Additionally, we conducted a theoretical analysis of RIN to identify the parameters that influence it. Detailed information can be found in Supplement 1, Part 4.

Ensuring VCSELs exceed ESD thresholds of 100 V is crucial for their reliability in real-world applications, particularly in environments where they may undergo frequent handling or integration into larger systems. We employ the Human Body Model (HBM) to assess the ESD tolerance of the chirped HCM VCSEL with both design I and design II, simulating an ESD event caused by human contact [40]. By subjecting the VCSEL to an ESD pulse of 125 V, we observe its robustness in withstanding such stress without experiencing any degradation. This exceptional level of ESD tolerance significantly mitigates the risk of device failure and enhances both longevity and performance stability within VCSEL-based systems. Both designs demonstrate excellent performance at high-speed data rates and in ESD tests, making them suitable for advanced communication applications. Additionally, we conducted other reliability tests, which also demonstrated exceptional stability after extended testing. Detailed information can be found in Supplement 1, Part 5.

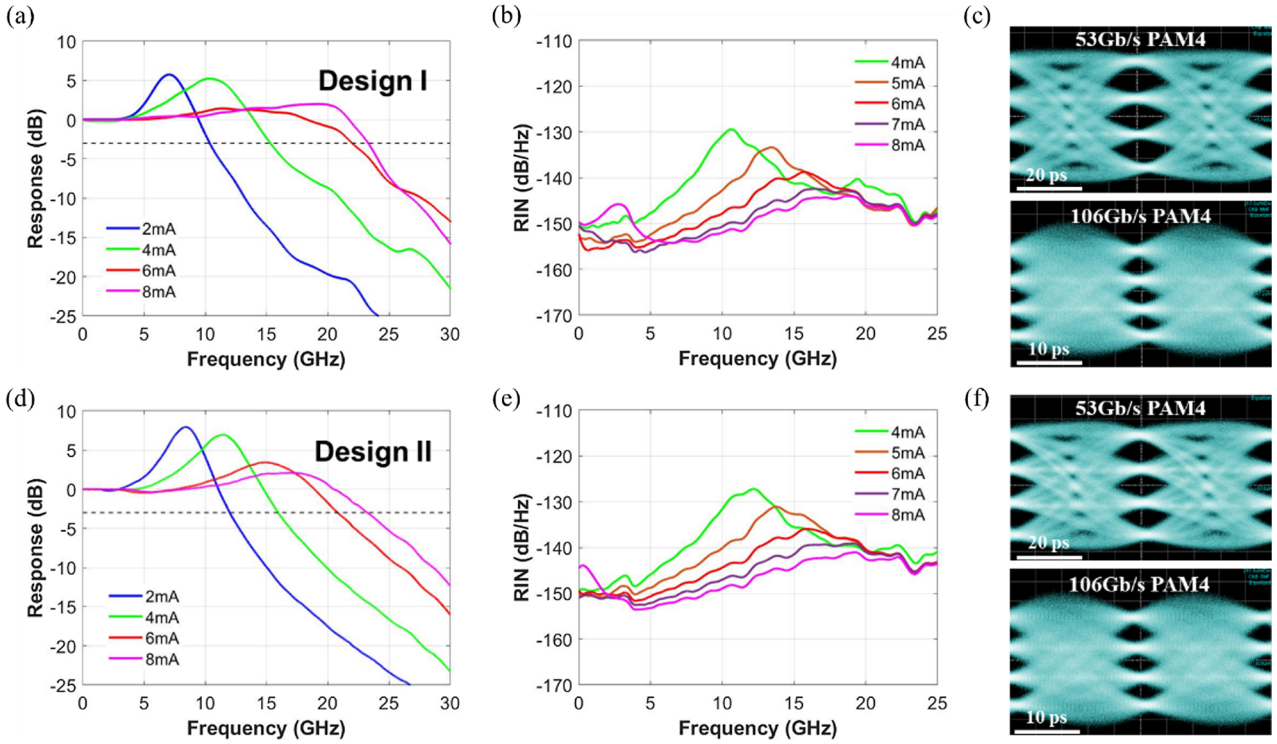

Fig. 5. Compares the S21, RIN, and PAM4 transmission eye diagrams for design I 1D and design II 2D chirped HCM VCSEL. (a), (d) The S21 is measured at room temperature under different bias currents, achieving a bandwidth of 23.4 GHz at an 8 mA current for both design I and design II. (b), (e) The RIN is measured at room temperature under various bias currents, with design I reaching approximately −144 dB/Hz and design II reaching approximately −142 dB/Hz at a maximum current of 8 mA. (c), (f) Open eye diagrams are obtained for PAM4 transmission data rates ranging from 53 Gbps to 106 Gbps for both designs, with design I achieving a TDECQ of 4.08 dB and design II achieving a TDECQ of 3.24 dB at 106 Gbps.

Table 1. Comparison with Other 850 nm Single-Mode VCSELs Reported in Recent Years

No	Year	Corresponding Author	Mechanism	D_A (μm)[a]	P_{MAX} (mW)[a]	I_{th} (mA)	SMSR (dB)	S21 3 dB Bandwidth (GHz)	Data Rate	Refs.
1	2021	Gong-Ru Lin	Metal mode filter	3		0.2	39	23.9	50 Gb/s PAM-4[b]	[2]
2	2022	Cunzheng Ning	Surface relief	4	1.1	0.2	40	22.5	50 Gb/s PAM-4	[6]
3	2022	Chao-Hsin Wu	Small aperture	2.5	1.9	0.8	40	29.1	48 Gb/s NRZ[b]	[33]
4	2023	Han-Yu Lin	Metal mode filter	5	0.9	0.4	30	Not mentioned	25 Gbit/s NRZ	[26]
5	2024	Fumio Koyama	Coupled cavity	4.5	1.8	0.8	30	21	48 Gb/s PAM-4	[18]
6	This work	Connie J. Chang-Hasnain	Chirped HCM	6	2.7	0.7	43	23.4	106 Gb/s PAM-4	—

[a] D_A is the aperture diameter of the VCSEL; P_{max} is the tested maximum output power.
[b] PAM-4 is pulse amplitude modulation-4; NRZ is non-return-to-zero; both are commonly used modulation schemes in data centers.

Table 1 compares our chirped HCM VCSEL with other 850 nm single-mode VCSELs reported in recent years. Our design offers several distinct advantages. First, with a larger optical aperture (OA) of 6 μm, our VCSEL ensures improved reliability, as smaller OAs are prone to issues like reduced electrostatic discharge (ESD) resistance and lower long-term stability. Moreover, our device achieves a significantly higher data rate, reaching 106 Gbps with PAM4 modulation, outperforming other approaches. Additionally, compared to some other methods for achieving single-mode operation, our fabrication process is much simpler. The lithographically defined chirped HCM enables efficient large-scale production, making it highly suitable for industrial implementation and mass production, without the need for complex regrowth or additional processing steps.

5. CONCLUSIONS

In this work, we present the first known report on an 850 nm single-mode VCSEL employing chirped HCM for continuous spatial control of mirror loss of the cavity. By incorporating a graded drop of reflectivity that corresponds to the intensity profile of the fundamental mode from the center to edge of the aperture, effective support is provided to the fundamental mode, while higher-order modes are suppressed. The chirped HCM VCSEL, with an oxide aperture size of 6 μm, demonstrates a threshold current of approximately 0.7 mA and achieves an SMSR exceeding 40 dB across a wide range of currents (2 mA to 8 mA) and temperatures (5°C to 75°C). The device's optical power output reaches 2.7 mW at 8 mA and has an ESD limit of 125 V according

to the HBM, exceeding the Telcordia Standards of 100 V. In small-signal modulation response (S21) testing, the −3 dB frequency is measured to be 23.4 GHz at 8 mA and RIN is found to be approximately −142 dB/Hz. Our single-mode chirped HCM VCSEL exhibits an open eye diagram during data transmission at a rate of 106 Gbps using single-mode fiber SM800.

Furthermore, the chirped HCMs can be easily integrated onto VCSELs, making them compatible with standard VCSEL processes and enabling mass production. This approach is wavelength scalable and applicable across a wide range of wavelengths. Therefore, our simplified design of chirped HCM VCSEL holds significant potential for various applications in optical interconnects, sensing, illumination, etc. In conclusion, we firmly believe that our proposed lithography-defined single-mode VCSEL will serve as a valuable tool in photonics research and development while opening up new avenues for exploration.

Funding. Shenzhen Science and Technology Innovation Program (501100017610) (KQTD20200820113053102, ZDSYS20220325163600001, JSGG20220831110404008, KJZD20231023100159002); Guangdong Major Talent Introduction Project (2021ZT09X328); Hetao Shenzhen-Hong Kong Science and Technology Innovation Cooperation Zone Program (HZQSWS-KCCYB-202203).

Acknowledgment. We thank the Berxel Photonics Co., Ltd. for fabrication support.

Disclosures. The authors declare no conflicts of interest.

Data availability. Data underlying the results presented in this paper are not publicly available at this time but may be obtained from the authors upon reasonable request.

Supplemental document. See Supplement 1 for supporting content.

REFERENCES

1. K. Iga, "Forty years of vertical-cavity surface-emitting laser: invention and innovation," Jpn. J. Appl. Phys. **57**, 08PA01 (2018).
2. M.-J. Li, K. Li, X. Chen, *et al.*, "Single-mode VCSEL transmission for short reach communications," J. Lightwave Technol. **39**, 868–880 (2021).
3. R. Puerta, M. Agustin, Ł. Chorchos, *et al.*, "Effective 100 Gb/s IM/DD 850-nm multi-and single-mode VCSEL transmission through OM4 MMF," J. Lightwave Technol. **35**, 423–429 (2016).
4. I.-C. Lu, C.-C. Wei, H.-Y. Chen, *et al.*, "Very high bit-rate distance product using high-power single-mode 850-nm VCSEL with discrete multitone modulation formats through OM4 multimode fiber," IEEE J. Sel. Top. Quantum Electron. **21**, 444–452 (2015).
5. J. Nanni, J.-L. Polleux, C. Algani, *et al.*, "VCSEL-based radio-over-G652 fiber system for short-/medium-range MFH solutions," J. Lightwave Technol. **36**, 4430–4437 (2018).
6. X. Zhang, G. Zhang, Y. Wen, *et al.*, "50 Gbit/s PAM4 data transmission over 500-m single-mode fiber using an 880-nm single mode VCSEL," IEEE Photon. Technol. Lett. **34**, 1210–1213 (2022).
7. K. Li, X. Chen, J. E. Hurley, *et al.*, "High data rate few-mode transmission over graded-index single-mode fiber using 850 nm single-mode VCSEL," Opt. Express **27**, 21395–21404 (2019).
8. H.-Y. Kao, C.-T. Tsai, S.-F. Leong, *et al.*, "Single-mode VCSEL for pre-emphasis PAM-4 transmission up to 64 Gbit/s over 100–300 m in OM4 MMF," Photon. Res. **6**, 666–673 (2018).
9. C.-Y. Peng, J. Qiu, T.-Y. Huang, *et al.*, "850-nm single-mode vertical-cavity surface-emitting lasers for 40 Gb/s error-free transmission up to 500 m in OM4 fiber," IEEE Electron Device Lett. **41**, 84–86 (2019).
10. P. Moser, J. A. Lott, P. Wolf, *et al.*, "85-fJ dissipated energy per bit at 30 Gb/s across 500-m multimode fiber using 850-nm VCSEL," IEEE Photon. Technol. Lett. **25**, 1638–1641 (2013).
11. E. Kapon and A. Sirbu, "Power-efficient answer," Nat. Photonics **3**, 27–29 (2009).
12. A. Babichev, S. Blokhin, A. Gladyshev, *et al.*, "Single-mode high-speed 1550 nm wafer fused VCSEL for narrow WDM systems," IEEE Photon. Technol. Lett. **35**, 297–300 (2023).
13. C. J. Chang-Hasnain, J. Harbison, G. Hasnain, *et al.*, "Dynamic, polarization, and transverse mode characteristics of vertical cavity surface emitting lasers," IEEE J. Quantum Electron. **27**, 1402–1409 (1991).
14. Y. Wu, C. Chang-Hasnain, G. Li, *et al.*, "Single-transverse mode, low threshold current vertical-cavity surface-emitting laser," IEEE Trans. Electron Devices **40**, 2116–2117 (1993).
15. T. Akutsu, T. Ushio, A. Matsutani, *et al.*, "Fabrication and characterization of VCSEL applying quantum well intermixing using spin-on-glass," Phys. Status Solidi **10**, 1452–1456 (2013).
16. A. Fischer, K. Choquette, W. Chow, *et al.*, "High single-mode power observed from a coupled-resonator vertical-cavity laser diode," Appl. Phys. Lett. **79**, 4079–4081 (2001).
17. K. Liu, Y.-F. Zhong, X.-W. Dong, *et al.*, "Single-mode vertical cavity surface emitting laser via high-order transverse mode expansion," J. Lightwave Technol. **41**, 6735–6740 (2023).
18. H. R. Ibrahim, A. Hassan, X. Gu, *et al.*, "Enhanced high-frequency modulation of single-mode 850nm VCSEL via dual transverse-cavity integration," IEICE Electron. Express **21**, 20230620 (2024).
19. P. Floyd, M. Peters, L. Coldren, *et al.*, "Suppression of higher-order transverse modes in vertical-cavity lasers by impurity-induced disordering," IEEE Photon. Technol. Lett. **7**, 1388–1390 (1995).
20. Y. Rao, W. Yang, C. Chase, *et al.*, "Long-wavelength VCSEL using high-contrast grating," IEEE J. Sel. Top. Quantum Electron. **19**, 1701311 (2013).
21. J.-W. Shi, Z.-R. Wei, K.-L. Chi, *et al.*, "Single-mode, high-speed, and high-power vertical-cavity surface-emitting lasers at 850 nm for short to medium reach (2 km) optical interconnects," J. Lightwave Technol. **31**, 4037–4044 (2013).
22. Y. Huang, X. Zhang, J. Zhang, *et al.*, "High single-fundamental-mode power VCSEL integrated with alternating aluminum content micro-lens," Appl. Opt. **57**, 7055–7059 (2018).
23. Y. Ji, M. Guan, J. Qi, *et al.*, "Transverse mode control in HCG-VCSEL," in *Conference on Lasers and Electro-Optics (CLEO)* (IEEE, 2020), pp. 1–2.
24. H.-P. D. Yang, F.-I. Lai, and J. Y. Chi, "Single-mode vertical-cavity surface-emitting lasers with a deep-etched half-ring-shaped holey structure," Appl. Phys Express **1**, 022004 (2008).
25. K. Li, Y. Rao, C. Chase, *et al.*, "Monolithic high-contrast metastructure for beam-shaping VCSEL," Optica **5**, 10–13 (2018).
26. H.-T. Cheng, S.-Y. Min, Y.-C. Yang, *et al.*, "Single-mode-VCSEL with a ring-shaped self-aligned recessed metal mode filter," IEEE Electron. Device Lett. **44**, 1316–1319 (2023).
27. H. J. Unold, S. Mahmoud, R. Jager, *et al.*, "Improving single-mode VCSEL performance by introducing a long monolithic cavity," IEEE Photon. Technol. Lett. **12**, 939–941 (2000).
28. D. Zhou and L. J. Mawst, "High-power single-mode antiresonant reflecting optical waveguide-type vertical-cavity surface-emitting lasers," IEEE J. Quantum Electron. **38**, 1599–1606 (2002).
29. M. S. Alias, S. Shaari, P. O. Leisher, *et al.*, "Single transverse mode control of VCSEL by photonic crystal and trench patterning," Photon. Nanostr. Fundam. Appl. **8**, 38–46 (2010).
30. K. D. Choquette, K. M. Geib, R. D. Briggs, *et al.*, "Single transverse mode selectively oxidized vertical-cavity lasers," Proc. SPIE **3946**, 230–233 (2000).
31. A. Liu, W. Chen, H. Qu, *et al.*, "Single-mode holey vertical-cavity surface-emitting laser with ultra-narrow beam divergence," Laser Phys. Lett. **7**, 213–217 (2010).
32. M. Vanzi, G. Mura, G. Marcello, *et al.*, "ESD tests on 850 nm GaAs-based VCSEL," Microelectron. Reliab. **64**, 617–622 (2016).
33. H.-T. Cheng, J. Qiu, C.-Y. Peng, *et al.*, "29 GHz single-mode vertical-cavity surface-emitting lasers passivated by atomic layer deposition," Opt. Express **30**, 47553–47566 (2022).
34. C. F. Mateus, M. C. Huang, Y. Deng, *et al.*, "Ultrabroadband mirror using low-index cladded subwavelength grating," IEEE Photon. Technol. Lett. **16**, 518–520 (2004).
35. C. J. Chang-Hasnain and W. Yang, "High-contrast gratings for integrated optoelectronics," Adv. Opt. Photon. **4**, 379–440 (2012).
36. F. Lu, F. G. Sedgwick, V. Karagodsky, *et al.*, "Planar high-numerical-aperture low-loss focusing reflectors and lenses using subwavelength high contrast gratings," Opt. Express **18**, 12606–12614 (2010).

37. X. Jia, Y. Ji, and C. Chang-Hasnain, "Single-mode VCSEL with double-focusing high-contrast gratings," in *CLEO: Science and Innovations* (Optica, 2020), paper STu4M.4.
38. M. C. Huang, Y. Zhou, and C. J. Chang-Hasnain, "A nano-electromechanical tunable laser," Nat. Photonics **2**, 180–184 (2008).
39. K. T. Cook, J. Qi, J. Wang, *et al.*, "Novel oxide spacer high-contrast grating VCSEL," in *CLEO: Science and Innovations* (Optica, 2018), paper STu3Q.6.
40. S. H. Voldman, *ESD: Failure Mechanisms and Models* (Wiley, 2009).